Proceedings of GT2009
ASME Turbo Expo 2009: Power for Land, Sea and Air
June 8-12, 2009, Orlando, Fl, USA

GT2009-59424

SIMULATION OF MIST FILM COOLING ON ROTATING GAS TURBINE BLADES

T. S. Dhanasekaran and Ting Wang
Energy Conversion and Conservation Center
University of New Orleans
New Orleans, LA 70148-2220

ABSTRACT

Film cooling technique has been successfully applied to gas turbine blades to prevent it from the hot flue gas. However, a continuous demand of increasing the turbine inlet temperature to raise the efficiency of the turbine requires continuous improvement in film cooling effectiveness. The concept of injecting mist (tiny water droplets) into the cooling fluid has been proven under laboratory conditions to significantly augment adiabatic cooling effectiveness 50-800% in convective heat transfer and impingement cooling. The similar concept of ejecting mist into air film cooling has not been proven in the laboratory, but computational simulation has been performed on stationary turbine blades. As a continuation of previous research, this paper extends the mist film cooling scheme to the rotating turbine blade.

For the convenience of understanding the effect of rotation, the simulation is first conducted with a single pair of cooling hole located near the leading edge at either side of the blade. Then a row of multiple-hole film cooling jets are simulated at stationary and rotational condition. Operating condition under both the laboratory (baseline) and elevated gas turbine conditions are simulated and compared. The effects of various parameters including mist concentration, water droplet diameter, droplet wall boundary condition, blowing ratio, and rotational speed are investigated. The results showed the effect of rotation on droplets at lab condition is minimal. The CFD model employed the Discrete Phase Model (DPM) including both wall film and droplet reflect conditions. The results showed that the droplet-wall interaction is stronger on the pressure side than on the suction side resulting in a higher mist cooling enhancement on the pressure side. The average mist cooling enhancement of about 15% and 35% are achieved on the laboratory and elevated conditions, respectively. This translates into a significant blade surface temperature reduction of 100-125 K with 10% mist injection at elevated condition.

Keywords: film cooling, surface curvature, mist cooling, heat transfer enhancement

NOMENCLATURE

BR	blowing ratio, $(\rho u)_c/(\rho u)_g$
C	concentration (kg/m^3)
c_x	axial velocity (m/s)
c_p	specific heat (J/kg-K)
D	mass diffusion coefficient (m^2/s)
d	film hole diameter (m)
D_m	midspan diameter (m)
GT	gas turbine
k	turbulence kinetic energy (m^2/s^2)
k_c	mass transfer coefficient (m/s)
h	convective heat transfer coefficient (W/m^2 - K)
h_{fg}	latent heat (J/kg)
Nu	Nusselt number, hd/λ
N	rotating speed (RPM)
P	pressure (N/m^2)
Pr	Prandtl number, ν/α
Re	Reynolds number, ud/ν
Ro	$\omega D / V$
S	source term
Sc	Schmidt number (ν/D)
T	Temperature (K)
U_m	peripheral blade velocity at midspan (m/s)
t	time (s)
x,y,z	coordinates

Greek

α	thermal diffusivity (m^2/s)
ϕ	flow coefficient
ε	turbulence dissipation rate (m^2/s^3)
η	adiabatic film cooling effectiveness, $(T_g-T_{aw})/(T_g-T_c)$
λ	thermal conductivity (W/m-K)
μ	dynamic viscosity (kg/m-s)
ν	kinematic viscosity (m^2/s)
ω	rotating speed (rad/s)
ρ	density (kg/m^3)
τ	stress tensor ($kg/m\text{-}s^2$)

Subscript

aw	adiabatic wall
c	coolant or jet flow
g	hot gas/air
p	particle or droplet
w	wall
sat	saturated
0	values for air film cooling without mist

1. INTRODUCTION

The film cooling technique is applied in modern gas turbine to protect the components such as turbine blades from hot flue gas. The inlet temperature of the gas turbine is being increased continuously to achieve high thermal efficiency, which correspondingly demands cooling techniques with increased high cooling effectiveness.

1.1 Film Cooling

There were numerous studies that focused on film cooling over flat surfaces with streamwise coolant injection in the past decades, eg. [1-3]; others studied film cooling in airfoil cascade environments to better simulate the flow and heat transfer mechanisms at engine conditions [4-6]. While most of the above studies were conducted at the stationary cascade blades, studies on rotating turbine are also abundant. Dunn et al. [7-8] studied the heat transfer on the vane, end–walls and rotors in a full stage rotating turbine using a shock-tunnel facility and thin-film heat flux gages. Abhari and Epstein [9] investigated the highly unsteady heat transfer on the rotors of transonic turbine. Mohendale et al. [10] studied the effects of high free-stream turbulence and upstream wake on heat transfer and film cooling of a rotor blade in a low speed wind tunnel facility. They concluded that high turbulence and wake increased the heat transfer slightly but significantly reduced the film cooling effectiveness for lower blowing ratio conditions. Takeishi et al. [11] employed the CO_2 mass transfer analogy technique to measure the local film cooling effectiveness on a rotor blade and found higher cooling effectiveness on the suction side than on the pressure side of the blade. They believed that this phenomenon was caused by the effect of the radial flow and strong mixing on the pressure surface. Suryanarayanan et al. [12] measured film-cooling effectiveness under rotation on the rotor blade platform and found that film-cooling effectiveness increased with an increase in the coolant-to-mainstream mass flow ratio for all turbine speeds. Higher turbine rotation speeds showed stronger spread of local film cooling coverage on the platform. Yang et al. [13] performed a numerical study of three-row film cooling on the leading edge of a rotor blade in a 1-1/2 turbine stage. They found that the film cooling and heat transfer showed an unsteady character due to the interaction of a rotating blade in a turbine stage and concluded that the film cooling effectiveness was high when the rotor blade was exposed to the high speed passage flow downstream of the stator, but decreased significantly when the rotor moves into the wake of the rotor blade.

1.2 Film Cooling with Mist

As the working gas temperature continuously increases to augment thermal efficiency, new cooling techniques are needed to surpass incremental improvements of convectional gas turbine cooling technologies. A promising technology to enhance film cooling is to inject water mist into the coolant flow. Each droplet acts as a cooling sink and flies over a distance before it completely vaporizes. This "distributed cooling" characteristics allows controlled cooling by manipulating different sizes of injected water droplets. The flow temperature reduces mainly due to droplet evaporation and partially due to larger specific heats of water and water vapor. Another important merit of employing mist film cooling is that some larger droplets can fly longer and evaporate farther into the downstream region where single-phase air film cooling becomes less effective. Li and Wang [14-15] simulated mist/air film cooling and showed that a small amount of mist injection (2% of the coolant mass flow rate) could increase the adiabatic film cooling effectiveness by about 30%~50% under low temperature, velocity and pressure conditions similar to those in the laboratory. They also investigated the effects of different flow parameters, injection hole configuration, and coolant supply plenum on the cooling effectiveness. Under the GT operating conditions with high temperature and high pressures, Wang and Li [16] they found the mist cooling enhancement was less attractive in terms of "enhancement percentage" (10~20%) than the cases with low pressure, velocity and temperature conditions. However, due to high surface temperature in the real gas turbine condition, relatively smaller percentage of cooling enhancement can result in larger wall temperature reduction, which is critical to significantly extend the life expectancy of gas turbine airfoils. To further simulate more closely to the actual GT operating conditions, Li and Wang [17] presented the mist/air film cooling heat transfer coefficient under conjugate condition by employing internal channel cooling beneath the blade surface. Result of conjugated 2-D cases indicated that reverse heat conduction from downstream to upstream along the solid wall was strong within a distance of 5 slot widths. Recently, Li and Wang [18] studied the curvature effect on mist film cooling. They found that the mist cooling enhancement was in the order of flat surface > pressure surface > suction surface> leading edge. Their simulation showed that the film cooling effectiveness increases of approximately 40% at the leading edge, 60% on the concave surface, and 30% on the convex surface could be achieved with 2% mist concentration.

The studies [14-18] on mist/air film cooling were conducted considering the turbine in stationary condition. But, considering the high-speed rotation in the real situation would make water droplets experience additional body forces such as centrifugal force and coriolis force apart from main forces like drag and gravitation, the present paper, as a continuation of previous studies, is focused on simulating mist film cooling under rotating turbine conditions.

2. NUMERICAL MODEL

2.1 Airfoil and Cooling Hole Configuration

For the present mist cooling analysis, the geometry of the one-and-half stage turbine conducted by Behr et al.[19] is used. The turbine had 3D twisted blades, which were designed by 2D blade profiles optimization with an inverse design scheme. The geometry details and flow parameters are given in Table. 1. For simplification, 2-dimensional turbine blades and stator blades are considered here based on the blade profiles used at mid section in Behr et al. [19] and equal number of rotor and stator blades (54) are assumed. Assuming the flow would be rotationally periodic, one rotor

blade and one stator blade are modeled for numerical study as shown in Fig. 1. The study is first conducted by using a single pair of holes to investigate the effect of rotation on mist transport without considering the effect of neighboring cooling jets. This pair of holes are placed at midspan of turbine leading edge: one at pressure side and one at suction side, respectively. These two holes are oriented at ± 35° with respect to the stagnation line as shown in Fig. 1. In this configuration of single pair of film holes , mist film cooling results are obtained as the baseline case with parameters listed in Table 2. In addition to investigating the rotation effect, simulations are also performed to study the effects of various mist concentrations, rotor rotational speeds, water droplet diameters and blowing ratios on mist film cooling performance.

After studying the film cooling injected from the single pair of film holes, a row of multiple film holes at the pressure side is simulated. The single-row configuration has five film cooling holes with 1mm diameter and the distance between the film holes is 7.5 mm, which gives the pitch-to-diameter ratio of 7.5. The film holes are oriented toward the tip at an orientation angle of 30° and zero inclination angle relative to the surface as shown in Fig. 1b. All the above mentioned calculations are considering the baseline (laboratory) working condition, i.e., at 1 atm, low inlet turbine temperature of 400 K, low inlet velocity of 7 m/s and low turbine rotational speed of 289 RPM. Finally, more realistic gas turbine working conditions are simulated at high rotational speed, high inlet velocity, high pressure and high inlet temperature with multiple film holes configuration.

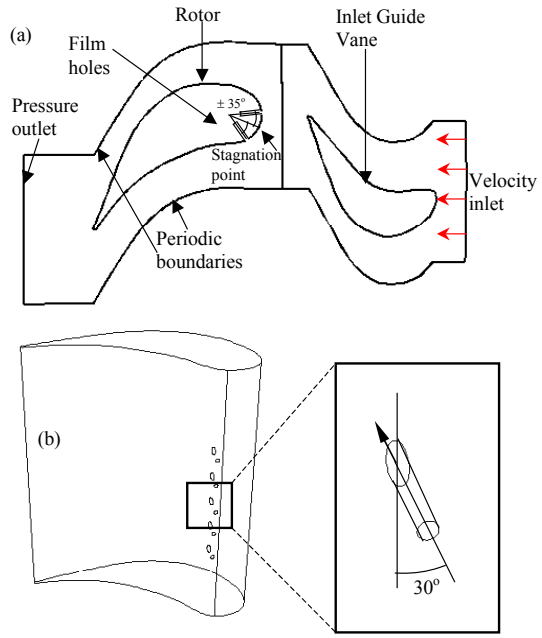

Figure 1 (a) Geometry and boundary conditions of the single stage turbine model and b) film cooling hole orientation and geometry of a single row configuration.

Table 1 Main parameters of a single-stage axial turbine considered

Rotor speed (RPM)	2700
Hub/Tip diameter (mm)	660/800
Flow coefficient ($\phi = c_x/U_m$)	0.63
No. of blades	54
Chord/pitch	1.41
Chord (mm)	59.85
Aspect ratio (span/chord)	1.17

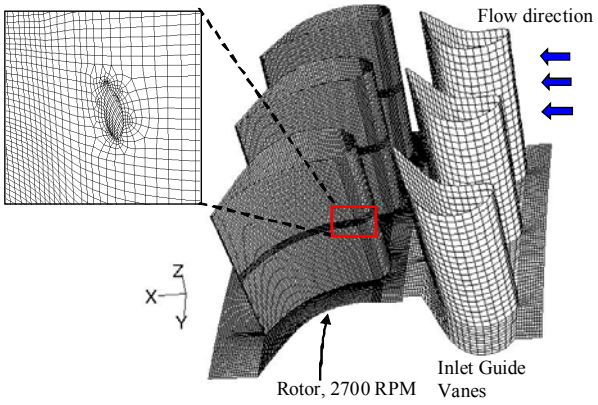

Figure 2 Elements on the rotor and stator. The film hole is located at the midspan of turbine blade (z = 0.635 m).

2.2 Numerical Method

A feasible method to simulate the film cooling with mist injection is to consider the droplets as a discrete phase since the volume fraction of the liquid is small (less than 0.1%) in this paper. The trajectories of the dispersed phase (droplets) are calculated by the Lagrangian method. The impacts of the droplets on the continuous phase are considered as source terms to the governing equations of mass, momentum, energy and species equations.

The following are the governing equations of mass, momentum, energy and species, which are based on time-averaged steady state conditions. (Please note that even the computation is conducted for rotating condition, the steady-state governing equations are used because only the rotating speed is added to the rotor domain without actually rotating the meshes. This will be further explained later).

$$\frac{\partial}{\partial x_i}\left(\rho u_i\right) = S_m \tag{1}$$

$$\frac{\partial}{\partial x_i}\left(\rho u_i u_j\right) = \rho \bar{g}_j - \frac{\partial P}{\partial x_j} + \frac{\partial}{\partial x_i}\left(\tau_{ij} - \rho\overline{u'_i u'_j}\right) + F_j \tag{2}$$

$$\frac{\partial}{\partial x_i}\left(\rho c_p u_i T\right) = \frac{\partial}{\partial x_i}\left(\lambda \frac{\partial T}{\partial x_i} - \rho c_p \overline{u'_i T'}\right) + \mu\Phi + S_h \tag{3}$$

$$\frac{\partial}{\partial x_i}\left(\rho u_i C_j\right) = \frac{\partial}{\partial x_i}\left(\rho D_j \frac{\partial C_j}{\partial x_i} - \rho\overline{u'_i C'_j}\right) + S_j \tag{4}$$

where τ_{ij} is the symmetric stress tensor. The source terms (S_m, F_j and S_h) are used to include the contributions from the dispersed phase. $\mu\Phi$ is the viscous dissipation and λ is the heat conductivity. C_j is the mass fraction of the species (j) in the mixture, and S_j is the source term for this species. D_j is

the diffusion coefficient. The diffusion term is used for bi-diffusion between water vapor and air mass. When the liquid evaporates into water vapor, it surrounds the liquid droplet. Then the water vapor will be transported away through convection and mass diffusion. Three species (oxygen, nitrogen and water vapor) are simulated in the paper.

The terms of $\rho\overline{u'_i u'_j}$, $\rho c_p \overline{u'_i T'}$ and $\rho\overline{u'_i C'_j}$ in the equations above represent the Reynolds stresses, turbulent heat fluxes, and turbulent concentration (or mass) fluxes, which should be modeled properly for a turbulent flow as seen in the film cooling of gas turbines. More detailed investigations and discussions on turbulence models and their effects on the simulation of mist cooling can be found in [20-22]. Typically, Reynolds Stress Model (RSM) turbulence model performed better and consistent with experimental data. The standard k-ε turbulence model is proven as robust with good results only next to the RSM model. Since RSM model requires an order of magnitude of computational time and in this study the primary goal is to compare the difference between mist and non-mist cases, the standard k-ε model is therefore used with the enhanced near-wall treatment with $y^+\approx 1$ to significantly reduce the computational time. The equations for the turbulent kinetic energy (k) and its dissipation rate (ε) are:

$$\frac{\partial}{\partial x_i}(\rho u_i k) = \frac{\partial}{\partial x_i}\left[\left(\mu + \frac{\mu_t}{\sigma_k}\right)\frac{\partial k}{\partial x_i}\right] + G_k - \rho\varepsilon . \quad (5)$$

$$\frac{\partial}{\partial x_i}(\rho u_i \varepsilon) = \frac{\partial}{\partial x_i}\left[\left(\mu + \frac{\mu_t}{\sigma_\varepsilon}\right)\frac{\partial \varepsilon}{\partial x_i}\right] + C_{1\varepsilon}G_k\frac{\varepsilon}{k} - C_{2\varepsilon}\rho\frac{\varepsilon^2}{k} . \quad (6)$$

The term G_k is the generation of turbulence kinetic energy due to the mean velocity gradients. The turbulent viscosity, μ_t, is calculated from the equation

$$\mu_t = \rho C_\mu \frac{k^2}{\varepsilon} \quad (7)$$

and the effective heat conductivity (λ_{eff}) and the effective diffusion coefficient are calculated by the following two equations, respectively.

$$\lambda_{eff} = \lambda + c_p\mu_t / Pr_t , \quad (8)$$

$$D_{eff} = D + \mu_t / Sc_t . \quad (9)$$

The constants $C_{1\varepsilon}$, $C_{2\varepsilon}$, C_μ, σ_k, and σ_ε used are: $C_{1\varepsilon}$ = 1.44, $C_{2\varepsilon}$ = 1.92, C_μ = 0.09, σ_k = 1.0, σ_ε =1.3 [23]. The turbulence Prandtl number, Pr_t, is set to 0.85, and the turbulence Schmidt number, Sc_t, is set to 0.7.

For the near wall region, the enhanced wall treatment is used, in which the standard two-layer model is combined with wall functions. To apply the two-layer approach, the computational domain is separated into a viscosity-affected region and a fully-turbulent region by defining a turbulent Reynolds number, Re_y, which is based on the distance from the wall.

$$Re_y = yk^{1/2}/\nu \quad (10)$$

where k is the turbulence kinetic energy and y is the distance from the wall. The flow is assumed in the fully turbulent region if $Re_y > 200$, and the k-ε model is used. Otherwise, the flow is in the viscosity-affected region, and the one-equation model of Wolfstein [24] is used. The turbulent viscosities calculated from the two regions are blended with a blending function (θ) to make the transition smooth.

$$\mu_{t,enhanced} = \theta\mu_t + (1-\theta)\mu_{t,l} \quad (11)$$

where μ_t is the viscosity from the k-ε model of high Reynolds number, and $\mu_{t,l}$ is the viscosity from the near-wall one-equation model. The blending function is defined so it is 0 at the wall and 1 in the fully-turbulent region. The wall functions are also enhanced by blending linear (laminar) and logarithmic (turbulent) laws-of-the-wall to make the applicability throughout the entire near-wall region.

To track the trajectory of droplets, the hydrodynamic drag, gravity and forces such as the "virtual mass" force, thermophoretic force, Brownian force, and Saffman's lift force are combined to affect the droplet motion. The energy equation for any individual droplet can be given as the following equation.

$$m_p c_p \frac{dT}{dt} = \pi d^2 h(T_\infty - T) + \frac{dm_p}{dt}h_{fg} \quad (12)$$

where h_{fg} is the latent heat. The convective heat transfer coefficient (h) can be obtained with an empirical correlation [25-26].

The evaporated mass is calculated by two modes: evaporation and boiling. During the evaporation mode, the evaporated mass change rate or vaporization rate is affected by the relative humidity in the air and is shown as Eq. (12) as been governed by concentration difference between droplet surface and the air stream,

$$-\frac{dm_p}{dt} = \pi d^2 k_c (C_s - C_\infty) \quad (13)$$

where k_c is the mass transfer coefficient, and C_s is the vapor concentration at the droplet surface, which is evaluated by assuming the flow over the surface is saturated. C_∞ is the vapor concentration of the bulk flow, obtained by solving the transport equations. When the droplet temperature reaches the boiling point, the following equation can be used to evaluate its evaporation rate [27]:

$$-\frac{dm_p}{dt} = \pi d^2\left(\frac{\lambda}{d}\right)(2.0 + 0.46Re_d^{0.5})\ln\left(1 + c_p(T_\infty - T)/h_{fg}\right)/c_p \quad (14)$$

where λ is the gas/air heat conductivity, and c_p is the specific heat of the bulk flow. Again, more details are documented in [20-22] for the model of discrete phase.

Stochastic method [28] is used to consider turbulence dispersion effect on droplets tracking. The droplet trajectories are calculated with the instantaneous flow velocity ($\bar{u} + u'$), and the velocity fluctuations are then given as:

$$u' = \varsigma\left(\overline{u'^2}\right)^{0.5} = \varsigma(2k/3)^{0.5} \quad (15)$$

where ς is a normally distributed random number. This velocity will apply during the characteristic lifetime of the eddy (t_e), a time scale calculated from the turbulence kinetic energy and dissipation rate. After this time period, the instantaneous velocity will be updated with a new ς value until a full trajectory is obtained. Since the results are sensitive to the time scale, an appropriate selection of the time scale is critical. In this study, the time scale is selected as 0.009 (k/ε). More detailed study about the effect of time scale on computational results and an appropriate selection of time scale is referred to [21].

2.3 Boundary Conditions

2.3.1 Airflow

The main flow and coolant flow are assumed to be dry air (zero humidity). In this simulation, the mist cooling effects are investigated at two different working conditions including baseline and elevated working conditions. In the lab condition, a lower turbine inlet absolute velocity of 7m/s (Re = 1.6x 10^5 based on the blade chord length) with 400 K are assigned. To maintain the designed flow coefficient of 0.63, the turbine rotation speed is reduced from 2700 RPM to 289 RPM. The lower inlet velocity is chosen in order to obtain comparable results with the previous study on this application [18]. At elevated working condition, the inlet velocity is raised to 103 m/s (Re = 38 x 10^5), the inlet temperature to 1500 K and the rotational speed to 2700 RPM to achieve the design flow coefficient of 0.63. The coolant jet inlet velocity is 10 m/s (Re_j = 3,760, based on the film hole diameter) with the inlet temperature of 300 K at the lab condition. The blowing ratio, is 1.88.

At elevated working condition, coolant jet inlet velocity is 22 m/s (Re_j = 13,750) and the blowing ratio is 0.5. The details of conditions and fluid properties for these two working conditions are given in Tables 2 and 3. The inlet turbulence is specified in terms of turbulence intensity 3% at mainstream inlet and 1% at the coolant flow inlet. The fluid at the rotor is defined as a moving reference frame with the angular speed equivalent to that of the blade. The computational faces at the two extreme ends in circumferential direction are assigned as rotational periodic condition. The flow exit of computational domain is assumed to be at a constant pressure of 1 atm. All the walls in the computational domain are adiabatic and have a no-slip velocity boundary condition.

2.3.2 Droplet injection

The uniform droplet size of 5μm is considered in the baseline case (Table 2) and the effect of distributed droplet diameter is also simulated for comparison. The mass ratio of mist over cooling airflow is 2% (about 2.74 x10^{-7} kg/s) in the baseline case. The number of mist injection points at coolant inlet depends on the number of computational elements at the inlet surface. In the present case about 120 injection points are placed. The trajectory number for stochastic tracking is chosen to be 10. The boundary condition of droplets at walls is assigned as "reflect" which means the droplets elastically rebound off once reaching the wall. The condition of droplet deposition at wall using wall-film model is also simulated and compared with "'reflect" model. Details about these two models are documented in Dhanasekaran and Wang [21]. At the outlet, the droplets just simply fly/escape from the computational domain.

Table 2 Conditions for the baseline and the elevated cases

	Baseline condition	Elevated condition
No. of film holes	1 and 5	5
Turbulence model	k-ε with standard wall function	k-ε with standard wall function
Blowing ratio	1.88	0.5
Mist ratio (wt.)	2%	10%
Rotational speed(RPM)	289	2700
Droplet wall boundary condition	Reflect	Reflect

Table 3 Air and water (liquid) properties at low baseline and elevated conditions

	Baseline (lab) condition	Elevated condition
Air	400 K 1atm	1500 K 15 atm
Density (kg/m^3)	0.871	3.483
Specific heat (J/kg-K)	1014	1230
Heat Conductivity (W/m-K)	0.0338	0.1
Dynamic viscosity (kg/m-s)	2.3 x 10^{-5}	5.5 10^{-5}
Kinematic viscosity (m^2/s)	2.6 x 10^{-6}	1.6 x 10^{-6}
Water		
Saturation temperature (K)	373	472
Specific heat (J/Kg- K)	4180	4490
Density (kg/m^3)	998	866
Latent heat (KJ/kg)	1950	2260
Others parameters		
Mist diameter (μm)	5	5
Main flow speed (m/s)	7	103
Jet flow speed (m/s)	10	22
Main flow temperature (K)	400	1500
Jet flow temperature	300	644
Re_{main}	1.6x10^5	38x10^5
Re_j	3,760	13,750
Flow coefficient (ϕ)	0.63	0.63
Rotational speed (RPM)	289	2700
Rotational number ($\omega D_m / c_x$)	3.16	2.0

2.3.3 Meshing and simulation procedure

The computational domain is constructed by structured hexahedral elements as shown in Figure 2. More intensive meshes are used on the rotor blade surface and near the cooling holes. The total number of 800,000 elements is used for the typical single row multiple film hole configuration. The rotating frame containing the rotor is simulated by

setting up two fluid zones using the "mixing plane technique." Two zones are the upstream guide vane and the rotor stage. In the mixing plane technique, both zones are treated as a steady-state problem. Flow field data from the adjacent zones are passed as boundary conditions that are spatially averaged at the mixing plane interface. This mixing removes any unsteadiness that would arise due to circumferential variations in the passage-to-passage flow field, thus yielding a steady-state result. Despite the simplifications inherent in the mixing plane model, the resulting solutions can provide reasonable approximations of the time-averaged flow field. The computation is carried out using the commercial CFD software FLUENT (Version 6.2.16) from Ansys, Inc. The simulation uses the segregated solver, which employs an implicit pressure-correction scheme and decouples the momentum and energy equations. The SIMPLE algorithm is used to couple the pressure and velocity. Second order upwind scheme is selected for spatial discretization of the convective terms and species. The computation is conducted for the main and coolant flow field (continuous phase) first. After obtaining an approximate converged flow field of the air the dispersed phase of droplet trajectories are calculated. At the same time, drag, heat and mass transfer between the droplets and the air are calculated.

Iterations proceed alternatively between the continuous and discrete phases. Ten iterations in the continuous phase are conducted between two iterations of discrete phase. Converged results are obtained after the residuals satisfy mass residual of 10^{-4}, energy residual of 10^{-6}, and momentum and turbulence kinetic energy residuals of 10^{-5}. These residuals are the summation of the imbalance for each cell, scaled by a representative of the flow rate. The computation was carried out in parallel processing on two dual-core Pentium clusters with 10 nodes and 6 nodes, respectively. It is found management is relatively easier to achieve more effective multi-task parallel processing by employing two separate clusters instead of one 16-node cluster.

3. RESULTS AND DISCUSSION

3.1 Results of Single Hole Film Cooling Configuration

3.1.1 Validation of CFD model

Due to unavailability of experimental work on the mist/air film cooling in the open literature, the CFD model has been validated against experimental results for the mist/steam impinging flow by Li et al. [20]. The details of the calibration of CFD model can be seen in Wang and Dhanasekaran [22]. For a quick reference, Fig. 3 shows both the standard k-ε and Reynolds Stress (RSM) turbulence model predicting well (within 5%) in comparison with the experimental results of wall temperature distribution on the target wall. Although the RSM model seems to fair a bit better, it takes 4-5 times longer to compute than the standard k-ε model. Considering the advantage of using RSM model does not seem to be as valuable as saving 80% of the computational time in the present study, the standard k-ε is chosen for this study.

The heat transfer results of multiple row impinging jets on a flat plate is shown in Fig. 3. The results show reasonable prediction of the wall temperature (T_{wall}) when impinged with steam only and with mist injection conditions within 5% of the experimental data based on the temperature scale, $T_w - T_{sat}$. The temperature span between 100°C (lowest value) and 320°C (approximately highest value) is used as the "temperature scale". This 5% prediction accuracy level is acceptable to this current study, so the CFD model is then applied on predicting the mist film cooling in a rotating vane-blade stage with a confidence that the uncertainty level is approximately of $\pm$ 10-15%.

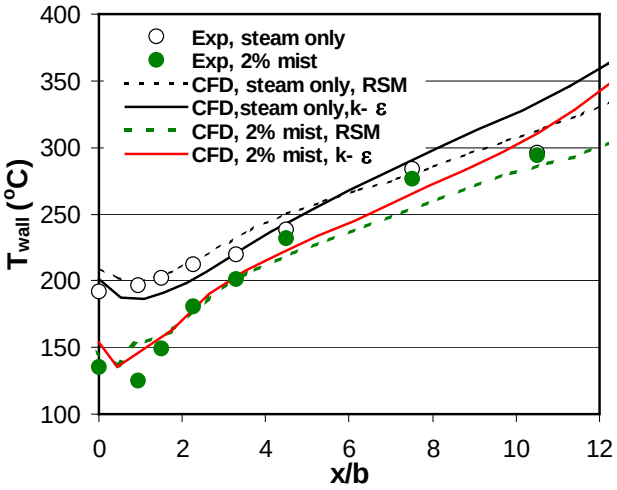

Figure 3 Qualification of mist cooling computational model by comparing with experimental results of a mist impinging jet conducted by Li, et al. [20].

3.1.2 Results of single hole film cooling configuration at baseline condition.

In evaluating film cooling performance, the adiabatic cooling effectiveness (η) is used, which is defined as :

$$\eta = (T_g - T_{aw})/(T_g - T_c) \qquad (16)$$

where T_g is the mainstream hot gas temperature, T_c is the temperature of the coolant (jet), and T_{aw} is the adiabatic wall temperature. The cooling effectiveness varies between zero (no cooling) and 1 (the wall temperature is the same as the coolant temperature).

Initially, a single film hole on pressure side of the turbine blade surface is considered. The results in Fig. 4a show that the adiabatic film cooling effectiveness is improved from s/d = 10 to 45, where s is the curvature length on pressure surface and d denotes the diameter of film hole. The locations s/d=10 and 45 are located near leading and trailing edge areas on the pressure side surface, respectively. The cooling effectiveness ratio (η_{mist}/η_o), or cooling enhancement, shown in the same figure clearly indicates that there is no observable cooling enhancement in the region immediately downstream of the film hole from

s/d = 0 to 10, but the cooling enhancement increases linearly downstream over the curved surface. The values presented in Fig. 4a are obtained from the local peak effectiveness values at various s/d locations. The spanwise cooling effectiveness for air-only and mist/air cases at stations s/d = 9.5, 20, 32 and 45 are shown in Figs. 4b to 4e respectively. The location of maximum effectiveness for air-only and mist/air cases differs in radial direction from stations s/d=20 to 45. Hence, the local peak values are used to showcase the cooling enhancement in Fig. 4a. In all the stations considered the location of peak effectiveness moves towards hub, once the mist is injected. The figures also show that the cooling effectiveness increases due to mist by 20% in the far downstream locations (s/d = 32 to 45).

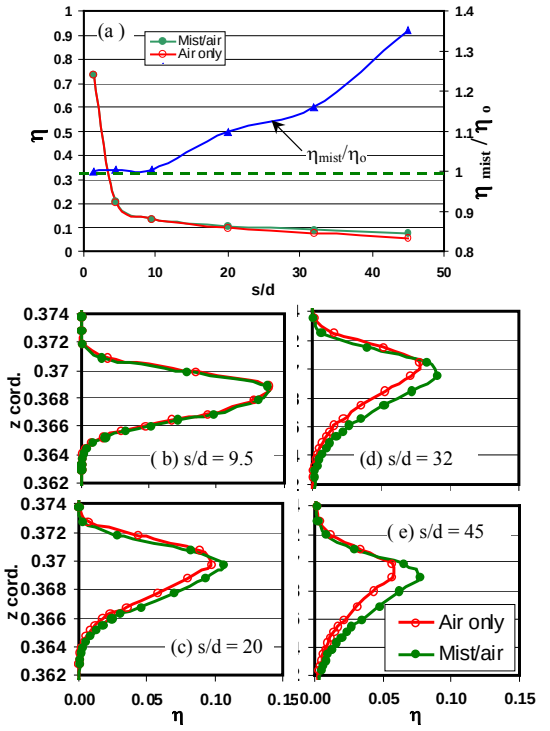

Figure 4 Heat transfer results of baseline case: Re = 1.6 x 10^5, 5µm, 2% mist, 289 RPM, baseline condition, cooling hole location is at z = 0.365.

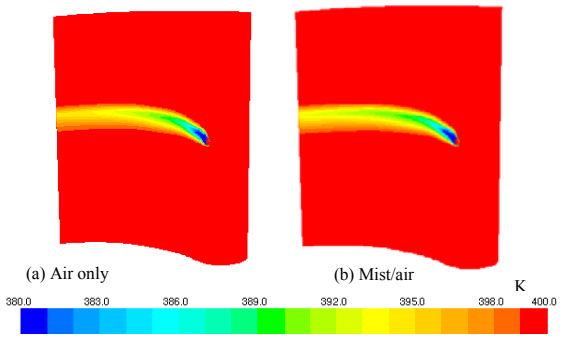

Figure 5 Temperature distribution on the pressure surface of the turbine of a single film cooling hole: a) Air only and b) mist/air (Re = 1.6x10^5, 5µm, 2% mist, 289 RPM, baseline condition).

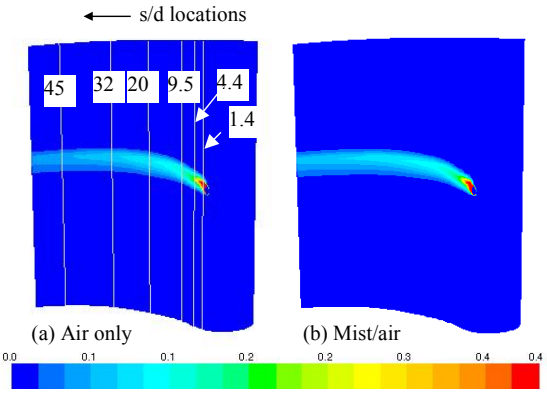

Figure 6 Adiabatic film effectiveness on the pressure surface of a single film hole: a) air only and b) mist/air (Re = 1.6 x 10^5, 5µm, 2% mist, 289 RPM, NWC).

The effective film cooling area (s/d = 10 to 45) where the predominant mist cooling enhancement takes place on the pressure surface of the turbine blade can be seen from the Figs. 5 and 6. The reason for the nil mist enhancement in the initial region (from s/d = 0 to 10) is explained with Fig. 7. The droplets (dots) and film cooling air (line) traces in the figure show that the coolant air is almost attached to the surface immediately after the injection location but the droplets are traveling farther away from the surface due to inertia force and centrifugal force induced by mass difference between air and water. This is the reason the mist enhancement is not seen in this region. Beyond s/d = 10 the droplets follow more closely to the air flow path and are attached to the pressure wall due to reduced centrifugal force as the droplet sizes continuously decrease with evaporation and interaction with wall surface. The decrease in droplet size can be seen from the figure as 5µm at the injection location and about 1.7µm at the turbine trailing edge. It can be noted that the droplets survive even after passing the blade surface. Due to the fact that the smaller droplets evaporates faster than larger droplets, the enhancement increases drastically downstream s/d = 35.

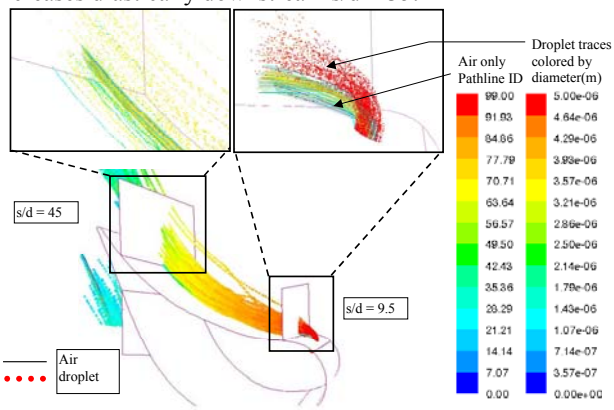

Figure 7 Air only film cooling pathlines and droplet traces: Re = 1.6 x 10^5, 5µm, 2% mist, 289 RPM, baseline condition (viewed from hub to tip).

Effect of mist on blowing ratio and Reynolds number

This study considers mass ratio of mist over cooling air flow of 2%, so the density increases approximately 2% also.

In the coolant channel, the liquid maintains as liquid, so the coolant velocity maintains about the same. Considering above two facts (2% increases of density and negligible change of velocity), the blowing ratio would vary approximately 2% if the correction of water mass were included.

When the water completely evaporates in the mainstream, the increased volume flow rate will increase the Reynolds number about 1-5% based on the fact that the mist is about 0.01% to 0.05% of the main mass flow rate (i.e. mist is 2 -10% of coolant flow mass, which is about 5% of the main flow mass). Since it takes time for the droplets to completely evaporate, the actual Reynolds number is difficult to track because the Reynolds number continues to change downstream of the injection hole depending on how much liquid droplets become vapor. It is understood that for a fair comparison, the effect of mist on Reynolds number could be isolated by using the same Reynolds number. However, as the Reynolds number undergoes continuously changes, it is felt that it would be easier to just consider the expanding volume flow rate caused by vaporized liquid droplets as one of the merits of mist flow and lump this enhancement into overall mist performance. This merit can be further realized by the reduced work used to pump liquid rather than compress vapor to the high-pressure environment in the turbine.

Effect of droplet wall boundary condition

In the baseline case the reflected Discrete Phase Model (DPM) wall boundary condition is used. The reflected model is usually appropriate when the wall is superheated higher than 35°C; however, in order to check if any water droplets deposit on the surface, the wall-film model is employed for 2% mist addition. The wall-film model allows liquid droplets to deposit on the wall surface and form a liquid film based on certain criteria (surface tension, surface superheat, etc.) If the wetting criteria are not satisfied, the droplets will be reflected back from the wall. More details on these boundary conditions can be found in [21]. Figure 8 shows that the cooling effectiveness arrived by the two models are almost same, which desensitizes the uncertainty of selection of droplet wall boundary condition. The reflect wall boundary condition is therefore employed for all cases in this study.

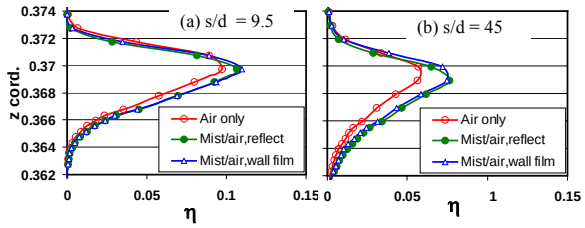

Figure 8 Effect of discrete phase model wall boundary conditions: reflect versus wall-film model (Re = 1.6 x10^5, 5μm, 2% mist, 289 RPM, baseline condition).

Effect of rotation

In order to clearly show the effect of rotation on the mist film cooling, simulations are also carried on the baseline case at stationary condition, i.e., 0 RPM rotational speed of turbine. Figure 9a shows that the mist enhancement is higher at 0 RPM than 289 RPM throughout the downstream location. Especially at the initial region from s/d = 0 to 10, noticeable enhancement is observed where the enhancement was nil for 289 RPM. Spanwise cooling effectiveness at s/b = 4.4, 20 and 45 clearly show in Figs. 9b to 9d that the location of maximum cooling for air-only film cooling shifts towards the hub regions when the turbine speed increases from 0 RPM to 289 RPM. This implies that the effect of rotation on the flow is strong by suppressing the inclined jet's penetration toward the tip. However, the location of maximum cooling doesn't change much after adding mist into air film. This suggests that the effect of rotation on the droplet is similar to on the air, so the droplets closely follow the air film jet. The reason for the higher cooling enhancement at 0 RPM can be explained with Fig. 10. From the static pressure distribution on the turbine blade in the figure, it is quite visible that the stagnation line has been shifted from leading edge (Figure 10 b) to the suction side (Figure 10 a) due to the shift in flow incidence angle with rotation. At the stationary case, the stagnation line is closer to the cooling hole, so the high static pressure in the stagnation region tends to suppress the momentum of film cooling air and droplets and causes the mist/air flow to attach to the surface immediately downstream the injection location. In contrary, with 289 RPM rotation, the droplets are separated from the wall as shown in Fig. 7. From the above discussion, it is evidenced that the forces acting on the droplet due to rotation of turbine blade doesn't affect the performance of mist cooling much and also observed that the closer the cooling hole location to the stagnation line, the higher the performance of mist cooling.

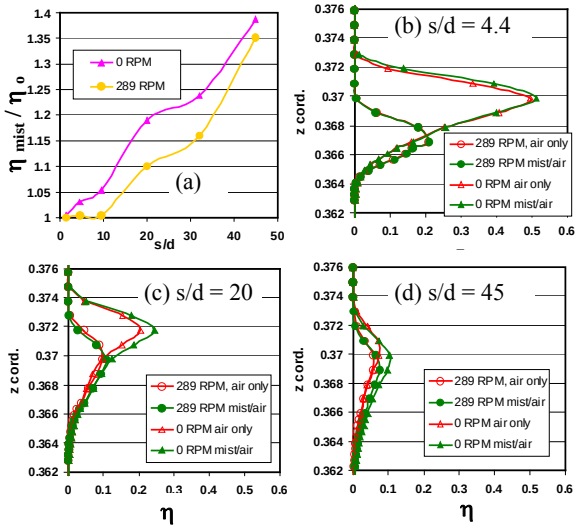

Figure 9 Effect of rotational speed on mist/air film cooling (Re = 1.6 x 10^5, 5μm, 2% mist, baseline condition).

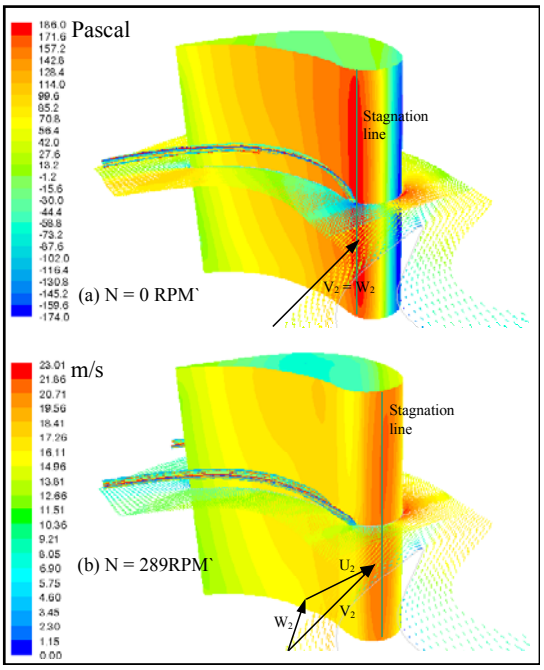

Figure 10 Static pressure distribution on the blade surface showing effect of rotation (Re = 1.6 x 10^5, 5μm, 2% mist, baseline condition). The color on the surface represents static pressure relative to the operating pressure at 101.325 Pascal. The velocity magnitude is represented by both color and vector length.

Effect of mist concentration

Figure 11 shows the influence of mist ratio on mist cooling performance including 2%, 10% and 20%. It is obvious from Fig. 11 that the cooling enhancement increases with increased amount of mist. It is worth to note that the cooling enhancement doesn't improve in the initial region from s/d = 0 to 10 for all the mist ratios. There is slight variation in the location of maximum effectiveness with mist ratio. The effect of centrifugal force on droplet becomes noticeable beyond 2% mist ratio in the far downstream region (Fig. 11c) The increase in mist cooling enhancement is drastic from 2% to 10% mist ratio, but not linearly proportional to the increased mist mass. For example, the enhancement in mid region for 2% mist ratio is about 25% and it increases to 100% due to increase in mist ratio to 10%. Further increase in mist ratio to 20% increases the enhancement to 150% (Fig. 11 a).

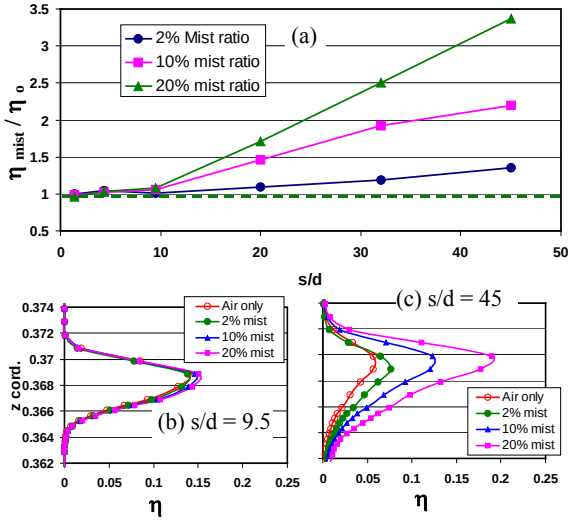

Figure 11 Effect of mist concentration (Re = 1.6 x 10^5, 5μm, 289 RPM, baseline condition).

Effect of blowing ratio

The effect of blowing ratio (BR) on the mist film cooling performance is shown in Fig. 12 including one higher (2.5) and one lower (0.5) blowing ratios apart from the baseline case (1.88). As far as the effect of blowing ratio for the air-only case is concerned, the cooling effectiveness increases as the blowing ratio reduces for the regions s/d = 0 to 20 and beyond s/d = 20 the trend is reversed i.e., the higher blowing ratio performs better than the lower ratio as shown in Fig. 12a. The result is consistent with Ou et. al [29], Ekkad et. al [30] and Yang et. al [13] When the mist is injected, lower blowing ratio performs better than higher blowing ratios throughout the downstream locations. The mist cooling enhancement ratio in Fig. 12a shows the drastic increase in cooling enhancement when the blowing ratio reduces from 1.88 (baseline case) to 0.5. For example the enhancement at s/d = 20 is about 10% with BR = 1.88 and the cooling enhancement value increases to 40% with BR = 0.5. It is observed from the flow insight that the particle injected at lower blowing ratio interacts with wall well immediately downstream of the injection hole than the higher blowing ratio cases as shown in Figs 12b to 12d. A larger droplet separation zone for higher BR is seen near the injection region.

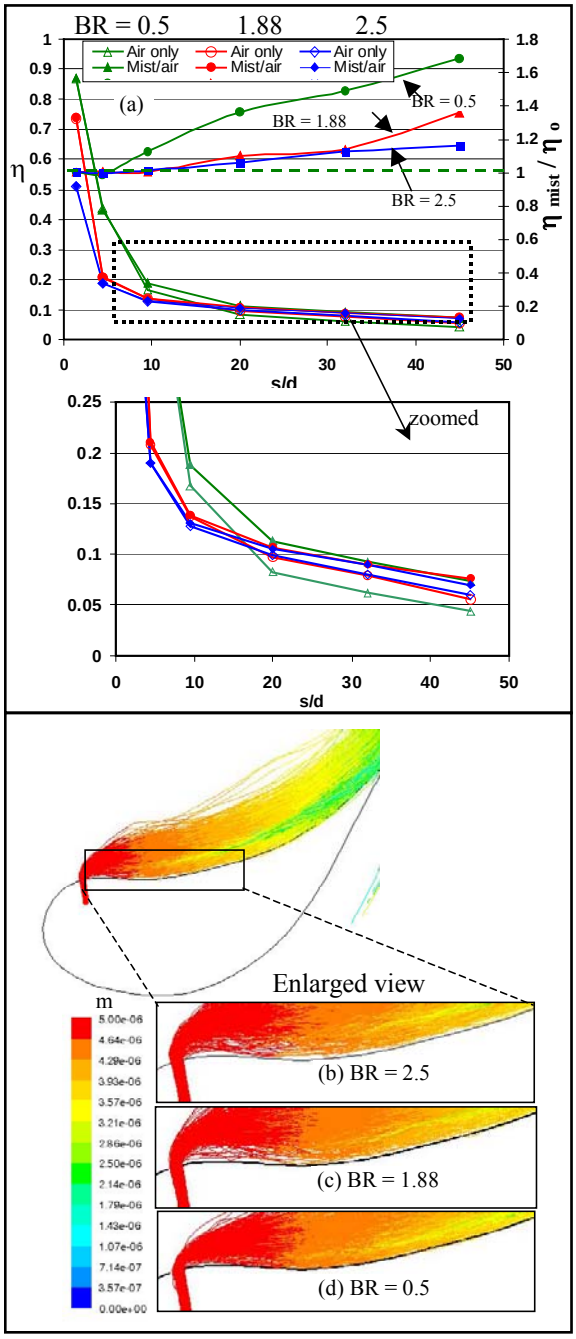

Figure 12 Effect of blowing ratio on air-only and mist/air film cooling (Re = 1.6 x 10^5, 5µm, 2% mist, 289 RPM, baseline condition).

Effect of droplet diameters

The effect of droplet diameter is studied by first injecting uniform diameters from 1µm to 20 µm to gain a clear understanding of the droplet size, followed by injecting distributed droplet diameters to simulate more closely to the actual condition as reported in the experimental studies. The Rosin-Rammler distribution function is used based on the assumption that an exponential relationship exits between the droplet diameter, d_d, and the mass fraction of droplets with diameter greater than d as:

$$Y_d = e^{-(d/d_m)^n} \qquad (17)$$

where d_m refers to the mean diameter (5µm) and n refers to the spread parameter. From the relationship, the spread parameter (2.4) is calculated and used to fit the size distribution into the CFD model. The results in Fig. 13 clearly show that increasing the droplet diameter reduces the mist cooling enhancement. As the diameter of droplet increases, the surface area per unit mass reduces causing a reduction in evaporation rate and hence the cooling effectiveness reduces. When the distributed diameter is injected, the cooling enhancement behaves between the small and large droplets. Overall, the distributed diameter droplets performs similar to lower constant droplet diameter (1µm) in the near injection region and similar to large constant droplets (20 µm) in the far field locations.

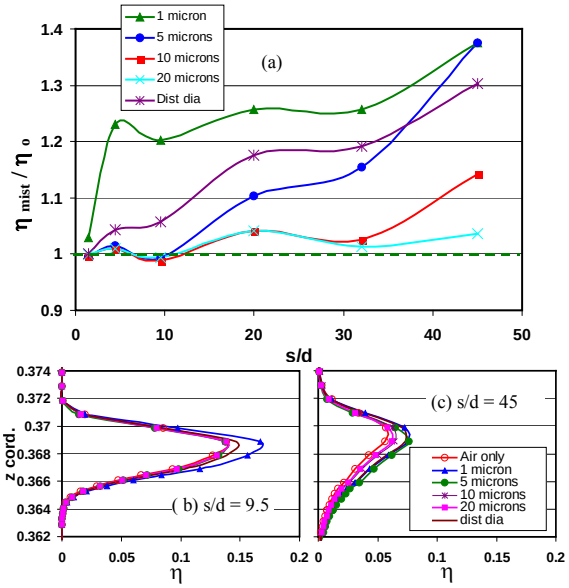

Figure 13 Effect of droplet diameter: Re = 1.6 x 10^5, 5µm, 2% mist, 289 RPM, baseline condition.

Comparison between suction and pressure sides

It is known that due to different flow and pressure fields over suction and pressure sides of a turbine blade, the film cooling performance on these sides is expected to be different. Figure 14 shows the comparison of film cooling performance between the suction and pressure sides for the baseline case. The film cooling with air-only case having higher peak cooling effectiveness value on suction side than on the pressure side. But, the integrated value over the pitch gives almost the same for the sides. When 2% mist is injected on either side, the peak mist cooling effectiveness on the suction side is still higher but the cooling enhancement is considerably higher in the pressure side as shown in Fig. 14a. For example, the cooling enhancement at s/d = 20 is about 10% on the pressure side but is only 5% on the suction side. From the flow pathlines and droplet track lines (not shown here), it was found that the droplets released from the suction side, unlike the pressure side, has relatively poor interaction with wall surface resulting in the

relatively lower mist cooling enhancement performance on the suction side. Figure 15 shows the peak cooling locations on both sides move towards the blade tip due to inclination injection, but the droplets on the pressure side, subjecting to the additional secondary flow effect, move further towards the tip than the suction side. The non-rotating case also shows the suction side has higher cooling effectiveness and pressure side has higher mist cooling enhancement.

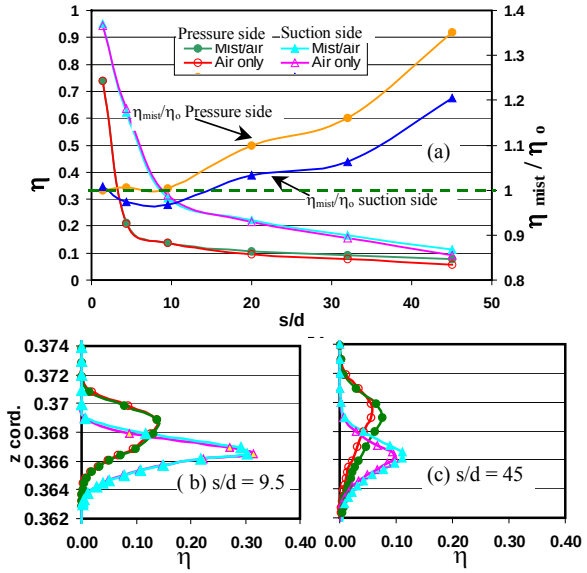

Figure 14. Effect of mist cooling on pressure and suction sides: Re = 1.6 x 10^5, 5µm, 2% mist, 289 RPM, baseline condition (film hole located at z = 0.365).

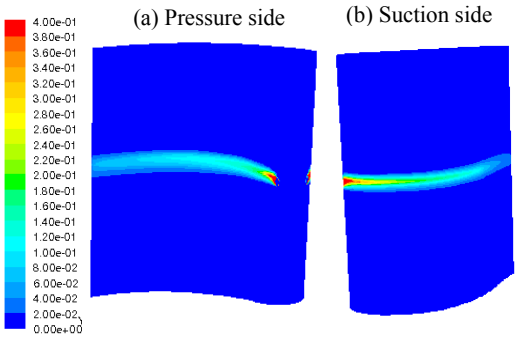

Figure 15 Distribution of effectiveness on pressure and suction surface: Re = 1.6 x 10^5, 5µm, 2%mist, 289 RPM, baseline case.

3.2 Results of Multiple Film Hole Configuration at the Laboratory Condition

The above sections described the mist cooling enhancement from a single pair of film holes located at the midspan of the turbine blade. The results have helped in understanding the pure mist enhancement without counting interactions between adjacent holes. In order to investigate the mist cooling enhancement in the real turbine, a single row of multiple-hole film cooling configuration on the pressure side is considered. The results are shown in Figs. 16 and 17. In general, the adiabatic film cooling effectiveness of multiple-hole configuration is slightly higher than the single-hole configuration (Fig. 17a) for both air-only and mist/air cases. Also, the peak cooling effectiveness diminishes along z direction (along the turbine blade span, Figs 17b and c). This may be due to the increased mixing with the hot main flow as a result of stronger secondary and corner flows created at the tip region than in the hub region. The increase in the cooling effectiveness is higher in the hub region than the tip region as shown in Figs. 17b and c. The effect of centrifugal force on the multiple-hole case is not pronounced as in the single-hole case, as can be seen on the peak cooling locations being near each injection spanwise z-location. Regarding the cooling enhancement, the multiple-hole configuration has almost identical enhancement values as the single-hole configuration (see Fig. 17a) ranging from 110% at s/d = 20 to 130% at s/d = 45. The cooling enhancement of multiple-hole case increases more linearly and smoothly than the single-hole case along the surface. Here, the enhancement at each x-location is calculated from the average of five spanwise cooling effectiveness peaks as shown in Figs. 17b and 17c.

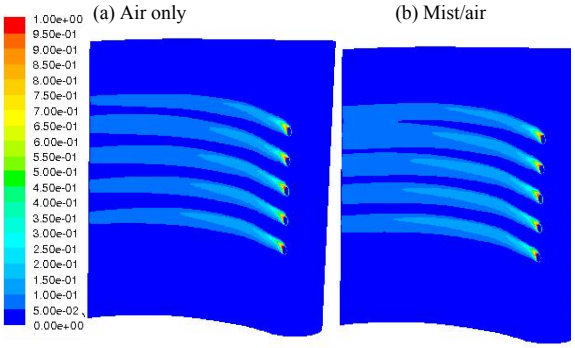

Figure 16 Distribution of multiple-hole film cooling effectiveness on pressure surface: Re = 1.6 x 10^5, 5µm, 2%mist, 289 RPM, baseline condition.

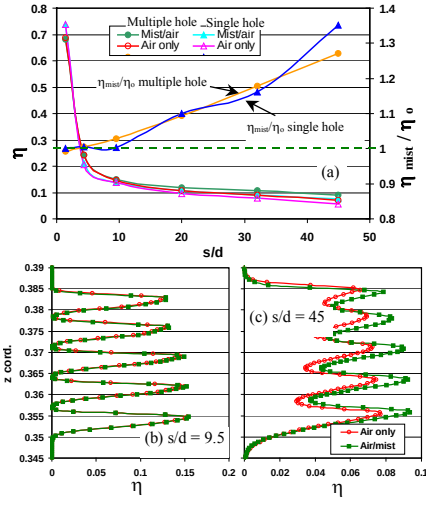

Figure 17 Adiabatic film cooling effectiveness of mist cooling for multiple-hole single row configuration: Re = 1.6 x 10^5, 5µm, 2% mist, 289 RPM, baseline condition.

3.3 Results of Multiple Film Hole Configuration at Elevated Working Condition

The results discussed so far have been conducted at low pressure, temperature and Reynolds number conditions, computation is then extended to simulate the mist cooling enhancement at elevated conditions which are one step closer to the real gas turbine environment. For this purpose, the inlet turbine temperature is raised to 1500 K, working pressure to 15 atm, inlet velocity to 103 m/s, Reynolds number to $38x10^5$, and rotation speed to 2700 RPM to reflect the actual gas turbine working condition. Due to more heat is to be absorbed to protect blade surface at elevated temperature, higher mist ratio of 10% is applied. Due to limited space, only one blowing ratio of 0.5 is presented. Table 3 provides a comparison of air and water properties and operating parameters between baseline and elevated conditions. The air density increases about 4 times at elevated condition, which will allow more droplets to suspend in and be supported by the air. The dynamic viscosity of air increases about 2.4 times which will reduce the slip velocity and therefore reduce heat transfer to the droplet via convection. This allows droplets to last longer to provide needed cooling further downstream. Both air heat capacity and water latent increase at elevated condition, which are beneficial to achieving more effective mist cooling.

Figure 18a shows that the air-only film cooling effectiveness (η) is lower at the elevated working condition than at the lab (baseline) condition in the initial s/d location less than 14, but becomes significant better in the farther downstream locations. The cooling effectiveness distribution at two representative locations of s/d = 9.5 and 45 are shown in Figs. 18b and c. The η distribution along z direction at s/d = 9.5 (Fig. 18b) for air-only film cooling case at elevated condition shows that the η value slightly reduces from hub to midspan but increases from midspan toward the tip region. This is quite different from the results obtained at the baseline condition (Fig 17b). One of the reasons for this behavior may be due to complex turbine passage flow at high rotational speed as the results of strong interaction with the secondary flows than it does at lower rotational speed.

The distinctive peak-valley η-distribution pattern in the earlier part of the film cooling coverage has been smeared and evened out downstream. This smeared cooling pattern was not seen earlier in the baseline condition (Fig. 17). The mist cooling enhancement at elevated condition is pleasantly higher than at the baseline condition. However, the cooling area covered by air-only film seems to cover more area near the tip region than mist cooling in the far-downstream area. As there are more spanwise film cooling holes to cover both the hub and tip regions in the real gas turbine blades, the reduction in the cooling area near the tip region is not a concern. As far as the mist cooling enhancement is concern, it is increased rapidly to 40% at s/d = 20 and gradually reduces to 25% at s/d = 45 in the elevated condition, which is translated into a significant blade surface temperature reduction of 100-125 K. This trend is quite different than that in the baseline case i.e., almost linearly increases from 0 to 28% (Fig. 18a).

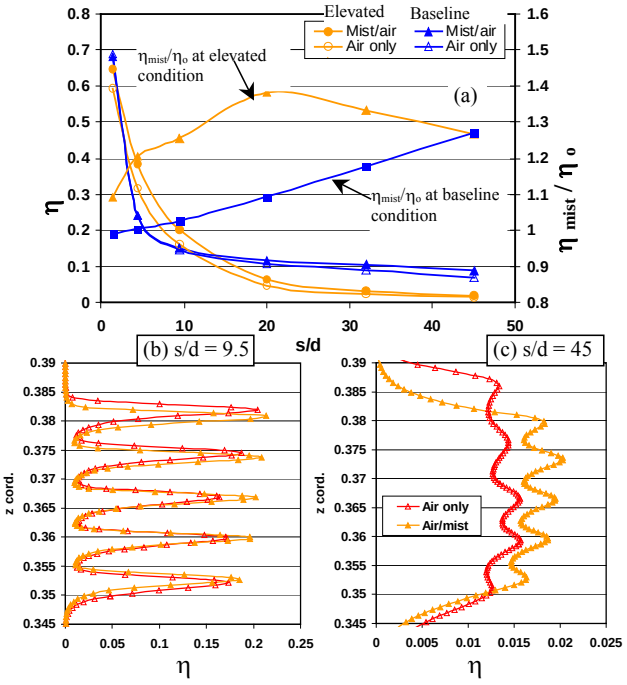

Figure 18 Mist film cooling performance at elevated condition: Re = 38 x 10^5, 5μm, 10% mist, 2770 RPM.

4. CONCLUSIONS

Motivated to provide significant cooling enhancement in the film cooling technique to protect the gas turbine blades, mist cooling technique is simulated with rotating turbine blade in this paper. The conclusions are:

- The mist cooling enhancement reduces with increase in rotational speed. The reduction in cooling enhancement is mainly contributed from change in the stagnation location due to change in incident angle corresponding to the increased RPM. Increase in rotational speed moves the stagnation region away from the film cooling hole on the pressure side and reduces droplet wall interaction in the near-hole region.
- Mist cooling enhancement is not linearly proportional to the mist ratio. For example, the mist cooling enhancement increases from 20% to 230% when the mist injection ratio increases from 2% to 20%.
- At laboratory (baseline) condition with 2% mist injection, the average cooling enhancement of about 30% is achieved on the pressure side and about 12% on the suction side. The droplet interaction with wall is higher on the pressure side than suction resulting in the difference in the mist cooling performance.
- Blowing ratio plays a critical role in the mist cooling enhancement. Reducing blowing ratio from 1.88 to 0.5 increases the mist cooling enhancement by 4 times in the baseline case.

- Small droplet diameter (1 μm) evaporates faster than larger droplets and provides mist cooling enhancement immediately downstream of the injection hole. As the diameter increases (from 5μm to 20μm) the cooling enhancement is almost nil in the initial regions from s/d = 0 to 10 and gradually increases beyond this point. In the practical situation of mist with distributed droplet diameters, the cooling enhancement is bounded by the performance of small and large droplets, i.e., a gradual increase in cooling enhancement right from s/d = 0 to far downstream locations.
- The mist cooling enhancement with the single film hole configuration and the multiple-hole configuration are almost identical in the present study except at the far downstream location beyond s/d = 40. The effect of rotation is less on the multiple-hole case than on the single-hole case with the spanwise cooling area staying centered along the injection location.
- At the elevated operating condition, an average of 35% mist cooling enhancement with an equivalent blade surface temperature reduction of 100-125 K has been predicted. More cooling is seen near the tip region. The peak-valley cooling difference evens out better in the far downstream area at elevated condition than at the lab condition.

Please note that since there are no experimental data available to verify the CFD results of this study, the readers are advised to consider the present results qualitatively.

ACKNOWLEDGMENTS

This study was supported by the Louisiana Governor's Energy Initiative via the Clean Power and Energy Research Consortium (CPERC) and administered by the Louisiana Board of Regents.

5. REFERENCES

[1] Goldstein, R. J., 1971, *Film Cooling : Advances in Heat Transfer*, Vol. **7**, Academic Press, New York, pp. 321–379.

[2] Walters, D. K. and Leylek, J. H., 1997, "A Detailed Analysis of Film-Cooling Physics—Part 1: Streamwise Injection With Cylindrical Holes", ASME Paper No. 97-GT-269.

[3] Mayhew, J. E., Baughn, J. W. and Byerley, A. R., 2003, "The Effect of Freestream Turbulence on Film Cooling Adiabatic Effectiveness", *Int. J. Heat Fluid Flow*, Vol. **24**, pp. 669–679.

[4] Drost, U. and Bolcs, A., 1998, "Investigation of Detailed Film Cooling Effectiveness and Heat Transfer Distributions on a Gas Turbine Airfoil", ASME Paper No. 98-GT-20.

[5] Zhang, L. J. and Pudupaty, R., 2000, "The Effects of Injection Angle and Hole Exit Shape on Turbine Nozzle Pressure Side Film Cooling," ASME Paper No. 2000-GT-247.

[6] Medic, G., and Durbin, P. A., 2002, "Toward Improved Film Cooling Prediction", *ASME J. Turbomach.,* Vol. **124**, pp. 193–199.

[7] Dunn, M.G., 1986, "Heat Flux Measurement for a Rotor of a Full Stage Turbine. Part I: Time averaged Results", *ASME Journal of Turbomachinery*, Vol. **108 (**1), pp.90-97.

[8] Dunn. M.G., George, W.K., Rae, W.J., Woodward, S.H., Moller, J.C. and Seymour, J.P., 1986, "Heat Flux Measurement for a Rotor of a Full Stage Turbine, Part II: Description of Analysis Technique and Typical Time-Resolved Measurements", *ASME Journal of Turbomachinery*, Vol. **108** (1), pp.98-107.

[9] Abhari, R.S. and Epstein, A.H., 1994, "An Experimental Study of Film Cooling in a Rotating Transonic Turbine", *ASME Journal of Turbomachinery*, Vol. **116** (1), pp.63-70.

[10] Mehendale, A.B., Ekkad, S.V. and Han, J.C., 1994, "Mainstream Turbulence Effect on Film Effectiveness and Heat Transfer Coefficient of a Gas Turbine Blade with Air and CO2 Film Injection", *International Journal of Heat and Mass Transfer*, Vol. **37** (10), pp. 2707-2714.

[11] Takeishi, K., Aoki, S., and Sato, T., 1992, "Film Cooling on a Gas Turbine Rotor Blade." *ASME Journal of Turbomachinery*, Vol. **114** (4), pp. 828-834.

[12] Suryanarayanan, A., Mhetras, S. P., M. T. and Han, J.C., 2006, "Film-cooling Effectiveness on a Rotating Blade Platform," ASME Turbo Expo 2006, Paper No 2006-90034.

[13] Yang, H., Chen, H.C. and Han, J.C.,2004, "Numerical Prediction of Film Cooling and Heat Transfer on the Leading Edge of A Rotating Blade in A 1-1/2 Turbine Stage", ASME Paper, IMECE 2004-59599.

[14] Li, X. and Wang, T., 2005, "Simulation of Film Cooling Enhancement with Mist Injection", *ASME Journal of Heat Transfer*, Vol. **128** (6), pp.509-519.

[15] Li, X., and Wang, T, 2007, " Effects of Various Modellings on Mist Film Cooling", *ASME Journal of Heat Transfer*, Vol. **129**, pp. 472-482.

[16] Wang, T., and Li, X., 2008, "Mist Film Cooling Simulation at Gas Turbine Operating Conditions", *International Journal of Heat and Mass Transfer*, Vol**. 51**, pp. 5305-5317, 2008.

[17] Li, X., and Wang, T., 2008, "Two-Phase Flow Simulation of Mist Film Cooling on Turbine Blades with Conjugate Internal Cooling", *ASME Journal of Heat Transfer*, Vol. **130**, pp.102901/1-8

[18] Li, X. and Wang, T., 2007, "Computational Analysis of Surface Curvature Effect on Mist Film Cooling Performance", *ASME Turbo Expo* 2007 (GT2007-27434), Montreal, Canada, 2007.

[19] Behr, T., Kalfas, A. I. and Abhari, R. S., 2007, "Unsteady Flow Physics and Performance of a one-and-1/2-Stage Unshrouded High Work Turbine", *ASME Journal of Turbomachinery*, Vol. **129**, pp. 348-358.

[20] Li, X., Gaddis, J. L., and Wang, T., 2001, "Mist/steam Heat Transfer in Confined Slot Jet Impingement," *ASME J. Turbomachinery*, Vol. **123**, pp. 161-167.

[21] Dhanasekaran, T. S. and Wang, T., 2008, "Validation of Mist/steam Cooling CFD Model in a Horizontal Tube", *Proceedings of ASME summer Heat Transfer Conference*, HT2008-5556280.

[22] Wang, T. and Dhanasekaran, T. S., 2008, "Calibration of CFD Model for Mist/Steam Impinging Jets Cooling", ASME Paper GT2008-50737, Turbo Expo2008, Berlin, Germany, June 9-13, 2008.

[23] Launder, B. E. and Spalding, D. B.,1972, "Lectures in Mathematical Models of Turbulence", Academic Press, London, England.

[24] Wolfstein, M., 1969, "The Velocity and Temperature Distribution of One-dimensional Flow with Turbulence Augmentation and Pressure Gradient", *Int. J. Heat Mass Transfer*, Vol. **12**, pp. 301-318.

[25] Ranz, W. E. and Marshall Jr. W. R., 1952, "Evaporation From Drops Part I", *Chem. Eng. Prog*, Vol. **48**, pp. 141-146.

[26] Ranz, W. E. and Marshall Jr, W. R., "Evaporation from Drops, Part II, Chem. Eng. Prog, Vol. **48**, pp. 173-180.

[27] Kuo, K. Y., 1986, Principles of combustion, *John Wiley and Sons*, New York.

[28] Fluent Manual, Version 6.2.16, 2005, Fluent, Inc.

[29] Ou, S., Mehendale, A. B. and Han, J. C., 1992, "Influence of High Mainstream Turbulence on Leading Edge Film Cooling Heat Transfer: Effect of Film Hole Row Location", *ASME J. Turbomachinery*, Vol. **114**, pp. 716-723.

[30] Ekkad, S. V., Han, J. C. and Du, H., 1998, "Detailed Film Cooling Measurements on a Cylindrical Leading Edge Model: Effect of Free-Stream Turbulence and Coolant Density", *ASME J. Turbomachinery*, Vol.**120**, pp.799-807.